Distributed Acoustic Sensing (DAS) for natural microseismicity studies: A case study from Antarctica

T.S. Hudson[1*], A.F. Baird[2], JM. Kendall[1], SK. Kufner[3], A.M. Brisbourne[3], A.M. Smith[3], A. Butcher[4], A. Chalari[5] and A. Clarke[5]

[1]Department of Earth Sciences, University of Oxford, Oxford, UK

[2]NORSAR, Kjeller, Norway

[3]NERC British Antarctic Survey, Cambridge, UK

[4]School of Earth Sciences, University of Bristol, UK

[5]Silixa Ltd, Elstree, UK (Affiliations should be preceded by superscript numbers corresponding to the author list. Each affiliation should be run in so that the full affiliation list is a single paragraph.)

Corresponding author: Thomas Hudson (thomas.hudson@earth.ox.ac.uk)

Key Points:

- Surface distributed acoustic sensing has limitations for microseismic detection/location compared to conventional seismic instrumentation
- Distributed acoustic sensing outperforms conventional geophones for source spectra and full-waveform source mechanism inversion
- 2D distributed acoustic sensing array geometries can be used as a multi-component sensor capable of measuring shear-wave splitting

Abstract

Icequakes, microseismic earthquakes at glaciers, offer critical insights into the dynamics of ice sheets. For the first time in the Antarctic, we explore the use of fibre optic cables as Distributed Acoustic Sensors (DAS) as a new approach for monitoring basal icequakes. Fibre was deployed on the ice surface at Rutford Ice Stream, in two different configurations. We compare the performance of DAS with a conventional geophone network for: microseismic detection and location; resolving source and noise spectra; source mechanism inversion; and measuring anisotropic shear-wave splitting parameters. The DAS arrays detect fewer events than the geophone array. However, DAS is superior to geophones for recording the microseism signal, suggesting the applicability of DAS for ambient noise interferometry. We also present the first full-waveform source mechanism inversions using DAS anywhere, successfully constraining the horizontal stick-slip nature of the icequakes. In addition, we develop an approach to use a 2D DAS array geometry as an effective multi-component sensor capable of accurately characterising shear-wave splitting due to anisotropy of the ice fabric. Although our observations originate from a glacial environment, the methodology and implications of this work are relevant for employing DAS in other microseismic environments.

Plain Language Summary

Icequakes are like small earthquakes but are caused by the movement of ice rather than two plates sliding past one another. They allow us to investigate glacier processes. For the first time in the Antarctic, we use lasers fired down fibre optic cables to detect and analyse icequake signals. This technique is called Distributed Acoustic Sensing (DAS). These fibre optic cables were laid on the surface of Rutford Ice Stream, Antarctica, in two different shapes. We compare the performance of DAS to conventional geophones for icequake detection and location, investigating the frequency of the earthquake source, investigating the physics that generates the icequake, and the effect of the ice fabric on the travel of seismic waves through ice. For our experiment, DAS is not as good as conventional geophones for detecting icequakes. However, DAS is better than geophones for looking at the frequency of an icequake and the physics that causes an icequake. It also allows us to investigate ice fabric properties in a similar way to geophones. Although our results are for icequakes at a glacier, the methods we use and our findings are relevant for using DAS in many other environments where small earthquakes occur.

1 Introduction

Distributed Acoustic Sensing (DAS) involves measuring strain along an optical fibre through time. As seismic waves propagate, they displace a medium elastically, producing a strain signal. This temporal strain signal is measured along the fibre, hence the name Distributed Acoustic Sensing. The typical spatial sampling resolution along a fibre is of the order of metres (Zhan, 2019), with cable lengths of 100s m to 100s km (Marra et al., 2018). DAS therefore has great potential for seismology since it can provide dense, sub-wavelength sampling of a seismic wavefield over a range of possibly 100s of km. Such sampling could provide a step-change in our understanding and observing capability of seismic processes.

Initially DAS was used in the oil and gas exploration industry, with fibre deployed in boreholes to image the subsurface with active seismic methods, such as Vertical Seismic

Profiling (VSP) (Daley et al., 2016; Daley et al., 2013; Mateeva et al., 2014). VSP methods are now applied in other environments, such as at glaciers (Booth et al., 2020). Recently, DAS has been applied to passive seismic investigations including: the study of tectonic earthquakes (Ajo-Franklin et al., 2019; Dou et al., 2017; Jousset et al., 2018; Lindsey et al., 2019; Marra et al., 2018; Sladen et al., 2019; Wang et al., 2018); ambient noise studies (Ajo-Franklin et al., 2019; Dou et al., 2017; Martin et al., 2018; Spica et al., 2020; Zeng et al., 2017); and microseismicity in a variety of settings including hydraulic fracture reservoir stimulation (Baird et al., 2020; Karrenbach et al., 2019; Stork et al., 2020; Verdon et al., 2020), geothermal seismicity (Li & Zhan, 2018), and alpine glacier icequakes (Walter et al., 2020).

Here we present a study of naturally occurring microseismicity at Rutford Ice Stream, Antarctica, using DAS surface arrays to investigate the potential of DAS for natural microseismicity studies more broadly. Rutford Ice Stream flows at a rate of 100s of metres per year (Rignot et al., 2011), providing a source of icequakes as ice slides over the underlying bed (Kufner et al., n.d.; Smith, 2006; Smith et al., 2015). An Antarctic glacier dataset is particularly suitable for such an investigation since Rutford icequake waveforms typically have high Signal to Noise Ratios (SNR) compared with other microseismic environments (Roeoesli et al., 2016; Smith et al., 2015). Furthermore, the velocity structure is approximately homogeneous, and therefore much simpler than volcanic or other settings. We first present a framework for initial detection and location of microseismicity using DAS, before demonstrating how DAS could be used for interrogating source physics and path effects. Source physics can help us understand basal sliding, while shear-wave splitting due to anisotropic path effects provides information associated with flow and deformation within the ice column. At each stage, we compare our results with conventional geophone data, quantifying the benefits, limitations and factors to consider in future deployments of DAS for studying natural microseismicity.

2 Methods

2.1 Overview of DAS and the data

DAS systems measure the strain-rate along an optical fibre by sending a finite-duration pulse of light from a laser along the cable, as in Figure 1. As photons travel along the cable, some undergo Rayleigh scattering from elastic collisions with particles in the fibre. As the cable deforms, the position of the collisions relative to the end of the cable changes, resulting in a change in the two-way travel-time of the photons scattered back to the source. This is observed as a modulation in the phase of the returning light. If the change in length of a section of fibre through time can be measured by this phase modulation, then the strain rate can be calculated. This technique is called optical time-domain reflectometry (Masoudi & Newson, 2016; Zhan, 2019). A subtle yet important additional concept is the gauge-length of the system, the length scale over which a change in strain is measured. The local change in strain is found by measuring the phase difference in the backscattered light from two closely separated points on the fibre. This measurement is proportional to the overall change in strain between these two points, the distance between which is referred to as the gauge length. Therefore, the gauge length controls the spatial resolution of the system, governing the response to different frequency signals (Dean et al., 2017). Here we use a Silixa iDAS^{TM} system (Parker et al., 2014) with a gauge-length of 10 m.

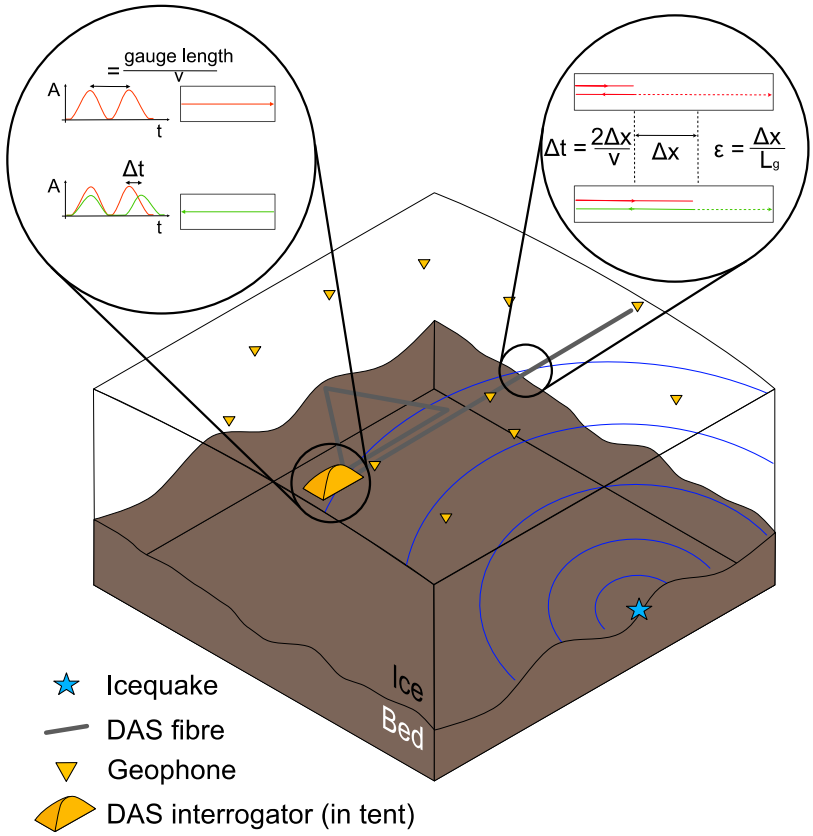

Figure 1. Schematic diagram showing the experiment arrangement and a simplified representation of how DAS works. The top left inset shows a simplified example of how the gauge-length corresponds to the input signal and how the backscattered light exhibits a phase shift. The top right inset shows the reflection from a single defect within one gauge-length along the fibre, without and with an external strain applied. L_g is the gauge-length and ε is the strain. The red line indicates the outgoing light and the green line the returning light. Note that the triangle and line configurations were not deployed at the same time.

The seismic data were acquired in January 2020, during the austral summer. The deployment consisted of a Silixa iDAS interrogator with a 1 km fibreoptic cable (see Supplementary Information), as well sixteen 4.5 Hz geophones with Reftek RT130 dataloggers, see Figure 2. The fibre was deployed in several geometric arrangements including a linear arrangement and a triangle, as shown in Figure 1 and Figure 2. The interrogator was located at the NE end of the line. To investigate coupling, we also deployed the cable in buried and unburied configurations. The sampling rate of both the geophones and the DAS is 1000 Hz. The local magnitude of icequakes in this study range from -1.9 to -0.9, calculated using the geophones.

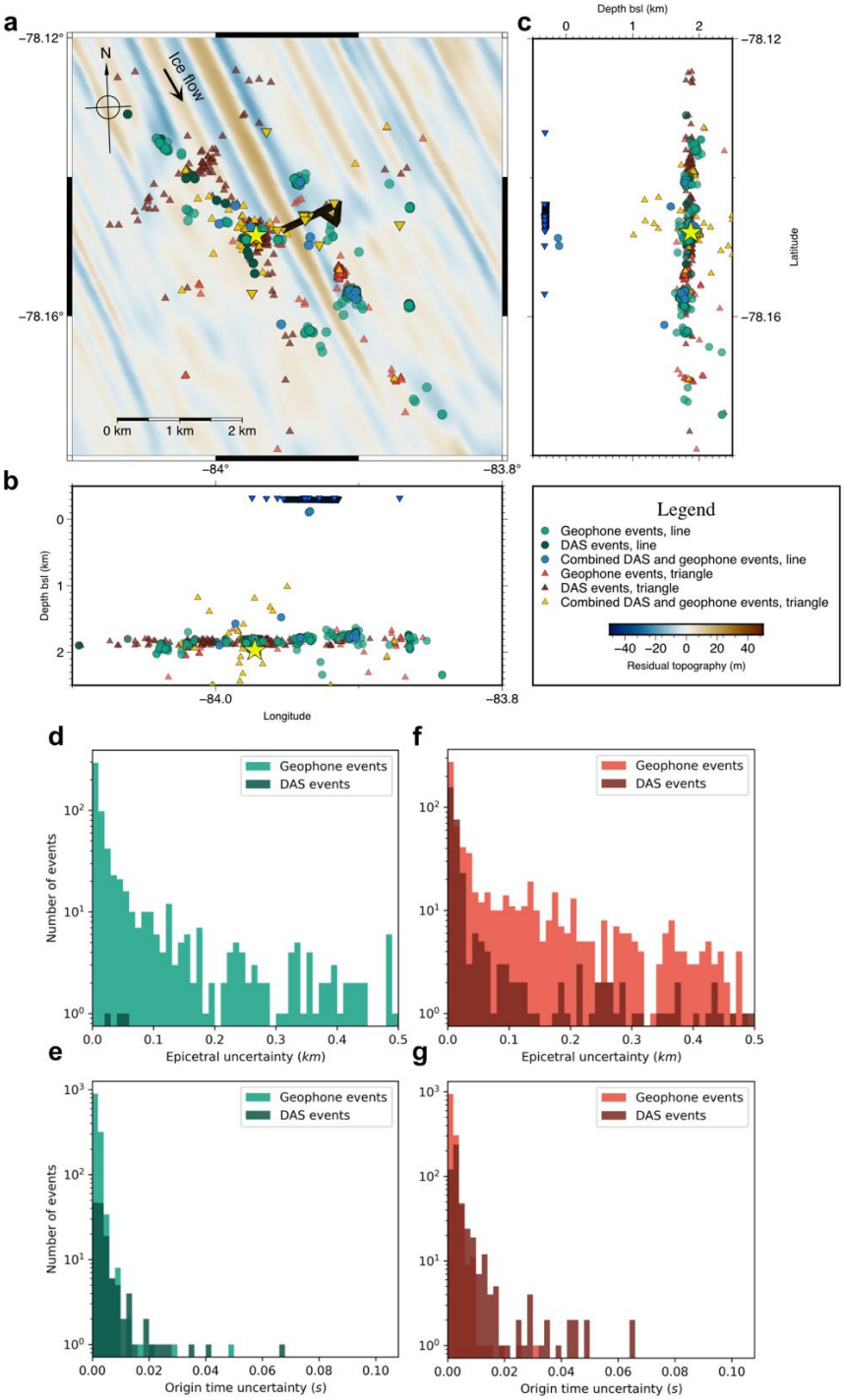

Figure 2. Icequake detections using DAS and geophones independently and together. a) Icequake locations, colored by instruments used for the detection. Inverted triangles indicate receivers, with the DAS fibre shown by the SSW to NEE line and triangle near the center of the figure. The yellow star corresponds to the example event shown in Figure 3. b) Same as a, but with the events plotted with depth vs. longitude. c) Same as b, but for depth vs. latitude. d) Histogram of epicentral uncertainty associated with the various networks used to detect and locate the icequakes, for the linear DAS fibre configuration. Note that epicentral uncertainties are clipped at an upper limit of 0.5 km for clarity. e) Histogram of origin time uncertainty associated with the various networks, for the for the linear DAS fibre configuration. f,g) Same as d,e, respectively, except for the triangle fibre configuration.

2.2 Microseismic detection method

There are various methods of detecting microseismicity using traditional instruments. These methods broadly fall into two categories, phase arrival-time detection methods and waveform-based migration methods. Phase arrival-time detection methods comprise of detecting P and S phase arrivals at a number of stations and using the arrival-time and velocity information to invert for the event hypocentre (Geiger, 1912). Phase arrivals can be obtained, for example, by using a Short-Term-Average to Long-Term-Average amplitude ratio (STA/LTA) algorithm to trigger event detections at each station (Allen, 1978; Withers et al., 1998). Waveform-based migration methods take a different approach, using the continuous full waveform information and the assumption of coherent energy arriving at multiple receivers in an array or network to back-migrate the energy. One example of this technique would be beamforming, where the wavefront of an event at the receivers in an array is used to determine the back-azimuth and distance of the event from the array (Capon, 1969).

Here, we apply a waveform-based migration method called QuakeMigrate (Hudson et al., 2019; Smith et al., 2020), which has previously been successfully used to detect microseismicity in a range of settings, including at glaciers (Hudson et al., 2019). QuakeMigrate approximates the energy associated with a phase arrival at a particular receiver as an onset function, which in our case is defined as a continuous STA/LTA function through time. Onset functions for each receiver are stacked and backpropagated through time and space, in order to search for a coalescence of energy corresponding to an event. One particular strength of this method is that although incoherent noise is back-migrated, it will not coalesce, therefore reducing the possibility of false detections. Another advantage of the method is that data from multiple instrument types can be combined once the waveform observations are approximated by onset functions, allowing for us to use both DAS and geophone time series data together in the detection and location algorithm. A further advantage of the QuakeMigrate algorithm is that it is open source, therefore allowing others to apply the methods demonstrated in this paper for other studies involving DAS, and hopefully improve upon our methods in the future.

Once the events have been detected and initially located, we refine the event locations using the non-linear earthquake relocation software, NonLinLoc (Lomax & Virieux, 2000). NonLinLoc provides quantification of the statistical spatial and temporal uncertainty of the icequakes, allowing us to quantify the performance of DAS only vs. geophone only vs. combined network detection and location.

2.3 DAS source mechanism inversion method

The earthquake source mechanism inversion used in this study is based upon the method described in Hudson et al. (2020) and available as the open source package SeisSrcInv (Hudson, 2020). Here we summarise the method, as applied to DAS data in this study, since there are a number of subtle alterations required. This specific DAS source inversion workflow is now implemented in SeisSrcInv.

The source inversion method is a full-waveform Bayesian source mechanism inversion, randomly sampling the model space millions of times in order to obtain an estimate of the posterior probability distribution. We constrain the source model to be a Double-Couple (DC) model, which is appropriate for the predominantly stick-slip seismicity observed at Rutford Ice Stream (Hudson et al., 2020; Kufner et al., n.d.; Smith et al., 2015). The DAS source inversion workflow is as follows:

1. First we down-sample the DAS data spatially. Due to the computational expense associated with calculating Green's functions and performing the source inversion, we only use every 10^{th} channel along the DAS cable to approximately sample the wavefield. This is found to be a sufficient resolution of spatial sampling, resulting in one waveform observed every 10 m, the same spatial scale as the gauge length of the DAS system.
2. We then filter the DAS data. We first apply an fk-filter with a wavenumber, k, of $0.04\ m^{-1}$ and a maximum frequency of $150\ Hz$. To remove surface wave noise from a generator, we also apply notch filters centred at 33 Hz and 66 Hz, with a bandwidth of 2.5 Hz.
3. Next we generate synthetic modelled waveforms, for comparison to the observed data, for each moment tensor component ($m_{xx}, m_{yy}, m_{zz}, m_{xy}, m_{xz}, m_{yz}$) for each DAS channel, for each event. These are calculated using the program fk (Zhu & Rivera, 2002). These synthetic waveforms are modelled for an isotropic, homogeneous ice medium overlaid with a 100 m firn layer of decreasing velocity.
4. Rutford Ice Stream has a strong anisotropic fabric (Harland et al., 2013; Smith et al., 2017), causing Shear Wave Splitting (SWS) that has to be accounted for. This can be done either by applying a linearization and time shift correction to the observed data, or by simulating the effect of SWS on the isotropic modelled S wave phases to produce anisotropic synthetic waveforms. Correcting for such effects is valid as long as the anisotropy is a path effect, and the source region can be assumed to be isotropic. We implement the latter method, approximating the effect of SWS on the synthetic DAS data by applying an average anisotropic splitting angle and a fast-slow S-wave delay time. We assume that the S-waves arrive at approximately normal incidence (vertical) to the surface, due to the firn velocity structure. We can then approximate the fast and slow S-wave arrivals in the North and East axes from the LQT coordinate system of the synthetics using the equations,

$$N_{fast} = -Q_{model}\cos(\theta)\cos(\phi) \quad ,$$
$$N_{slow} = Q_{model}\cos(\theta)\sin(\phi) \quad ,$$
$$E_{fast} = T_{model}\cos(\theta)\cos(\phi) \quad ,$$
$$E_{slow} = -T_{model}\cos(\theta)\sin(\phi) \quad ,$$

   where θ is the azimuthal angle from the source to the receiver and ϕ is the average anisotropic splitting angle. These can then be combined into single N and E traces using,

$$N_{model,aniso}(t) = N_{fast}(t) + N_{slow}(t+\delta t) \quad ,$$
$$E_{model,aniso}(t) = E_{fast}(t) + E_{slow}(t+\delta t) \quad ,$$

   where δt is the fast-slow S-wave delay time.
5. Once the simulated anisotropy has been applied to the synthetic modelled data, the North and East model components can then be rotated into the DAS axis, $DAS_{model}(t)$, given by,

$$DAS_{model}(t) = N_{model,aniso}\cos(\gamma) + E_{model,aniso}\sin(\gamma) \quad ,$$

where γ is the angle of the DAS fibre clockwise from North. It is important that this angle corresponds to the positive strain-rate direction along the fibre, as defined by the DAS interrogator.

6. The observed DAS data is in units of strain rate, and the modelled DAS data is in units of velocity. In order to compare the modelled data to the observations, one therefore has to convert all the data either into strain rates or velocities. We opt for converting the synthetic modelled data into strain rate. The axial strain-rate, $\dot{\varepsilon}_x$, the native measurement of DAS, by differentiating spatially, as given by,

$$\dot{\varepsilon}_x = \frac{\partial v_x}{\partial x} = \frac{\partial DAS_{model}(t)}{\partial x} \quad ,$$

where v_x is the velocity and x is the distance in the direction parallel to the cable. To make the modelled strain-rate consistent with the DAS, this differentiation should be applied over a length scale equal to the gauge length.

7. Now that the observed and modelled data are in the same coordinate system and both in units of axial strain-rate, they can be compared to one another in a source mechanism inversion. We do this for a DC-constrained inversion with 1×10^6 samples.

2.4 DAS shear-wave splitting inversion method

Rutford Ice stream is strongly anisotropic, as evidenced by the presence of shear-wave splitting (Harland et al., 2013; Smith et al., 2017). Shear-wave splitting provides a measure of the anisotropy along the ray path between the source and the receiver, which can be characterised by a delay time, *dt*, between the fast and slow S wave arrivals, and the polarization, ϕ_f, of the fast S wave (e.g. Wuestefeld et al. (2010)). Shear wave splitting is typically estimated using 3 component particle motion analysis on geophones. However, such an approach is not possible with linear DAS data because of its single component nature and because it measures strain-rate rather than particle motion. Shear wave splitting has previously been observed and analysed using DAS in strongly anisotropic shales (Baird et al., 2020). In that case, the S waves arrive as two distinct arrivals allowing dt to be measured. In that example the anisotropy was known to have a relatively simple Vertical Transverse Isotropy (VTI) symmetry fabric such that determining the polarisation was straightforward. However, at Rutford the anisotropy has a more complicated orthorhombic symmetry (Smith et al., 2017), making determination of the polarization using DAS challenging.

Here we describe a methodology for estimating shear wave splitting using the triangular DAS array. The motivation for this is to provide a proof of concept demonstrating that a 2D DAS geometry can be effectively used as a multi-component sensor capable of measuring shear-wave splitting. Using the triangular array partially alleviates for the inherent single component nature of DAS fibre because it records strain in a 2D plane rather than a 1D line, albeit with measurements at different orientations not at precisely the same location. However, if we assume that at the scale of the array the S-waves can be approximated as plane waves, we can approximate the triangular array as a point sensor, by correcting for the spatial distribution, similar to the approach of Innanen et al. (2019). We then need to determine how the amplitudes recorded on the three sides of the array relate to the polarization of the S waves. The strain sensitivity pattern of an S wave depends on both the orientation of the ray slowness vector (i.e. wavefront propagation direction) and of the polarization vector (Baird et al., 2020; Benioff, 1935; Karrenbach et al., 2019). Thus, if we

can first estimate the orientation of the slowness vector, we can then invert for the polarization that best fits the observed data.

We illustrate the proposed methodology using an example icequake shown in Figure 3, which clearly shows the differing moveout observed on each side of the array. The anisotropy inversion processing steps to find the fast-slow S wave delay time and polarization are as follows:

1. We first divide the array into the three linear segments of the triangle and apply a slant stacking processing technique to stack data over various possible linear velocities represented by apparent slowness values. These are normalised by the number of channels in the stack to preserve amplitudes (see Figure 3). This single processing step achieves several requirements needed for the inversion: (1) it provides an estimate of one of the components of the slowness vector, which is required to estimate the propagation direction in order to forward model the strain sensitivity; (2) it reduces the varying travel times over the length of the array to a single point measurement at its midpoint; and (3) it aids in the identification and picking of the two S phases by separating them by their apparent slowness where otherwise they might be partially overlapping.
2. The fast and slow S waves are then picked in the slowness-time domain, with the peak amplitude of the phase immediately after the pick taken as the recorded strain-rate amplitude of that arrival (see Figure 3d). The travel time difference between the fast and slow waves provides an estimate of the shear-wave splitting delay time *dt*. This analysis is then repeated for each side of the triangle, with the estimated *dt* at the midpoint of the array taken as the average of all those recorded on each side.
3. Next we need to determine the orientation of the slowness vectors (i.e. the wavefront propagation directions) of the two S waves. Since we have measured the apparent slowness of each S wave on the three sides of the array, we can apply a least squares inversion to solve for the best fitting horizontal slowness components. One should note that this slowness method provides an independent estimate for the azimuth of the source epicentre relative to the array from the hypocentral locations derived earlier in this study. This independence from our detection and location method is important because our original locations could be biased by the assumption of no anisotropy.
4. Once we have determined the S wave slowness vectors, we can then perform an inversion to obtain the fast and slow S wave polarizations. The strain tensor $\mathbf{e_S}$ associated with an S wave propagating in the x_1 direction and polarized in the x_3 direction has the form

$$\mathbf{e_S} = \begin{bmatrix} 0 & 0 & e_S \\ 0 & 0 & 0 \\ e_S & 0 & 0 \end{bmatrix} ,$$

where the scalar factor e_S determines the overall amplitude of the strain. Thus, to simulate the DAS response to an S-wave with arbitrary propagation and polarization directions, we need to rotate this tensor into the appropriate orientation, and project the resulting tensor onto the fibre geometry. To eliminate the need to solve for e_S, we can instead model the ratio of strain on different sides of the array. Since we have already estimated the azimuth and emergence inclination in step 3, this then leaves only the polarisation to be determined, which is described by a rotation about the propagation axis. Applying the approach to our example, we choose side two of the array as our reference (see Figure 3) and normalize the recorded strain amplitudes on each side by the amplitude on side two (i.e. $A_{side\ 1}/A_{side\ 2}$ and $A_{side\ 3}/A_{side\ 2}$). We then

apply a least squares inversion to solve for the S polarization that minimises the misfit between the modelled and observed amplitude ratios. We apply separate inversions for the fast and slow S waves.

In order to compare our splitting measurements with previously published splitting results from Smith et al. (2017), we convert *dt* to a percentage difference in fast and slow S velocities dv_S, by using the formula from (Wuestefeld et al., 2010),

$$dv_S = 100\frac{v_{Smean}dt}{r} \quad ,$$

where *r* is the source-receiver distance and v_{Smean} is the mean S-wave velocity along the full path.

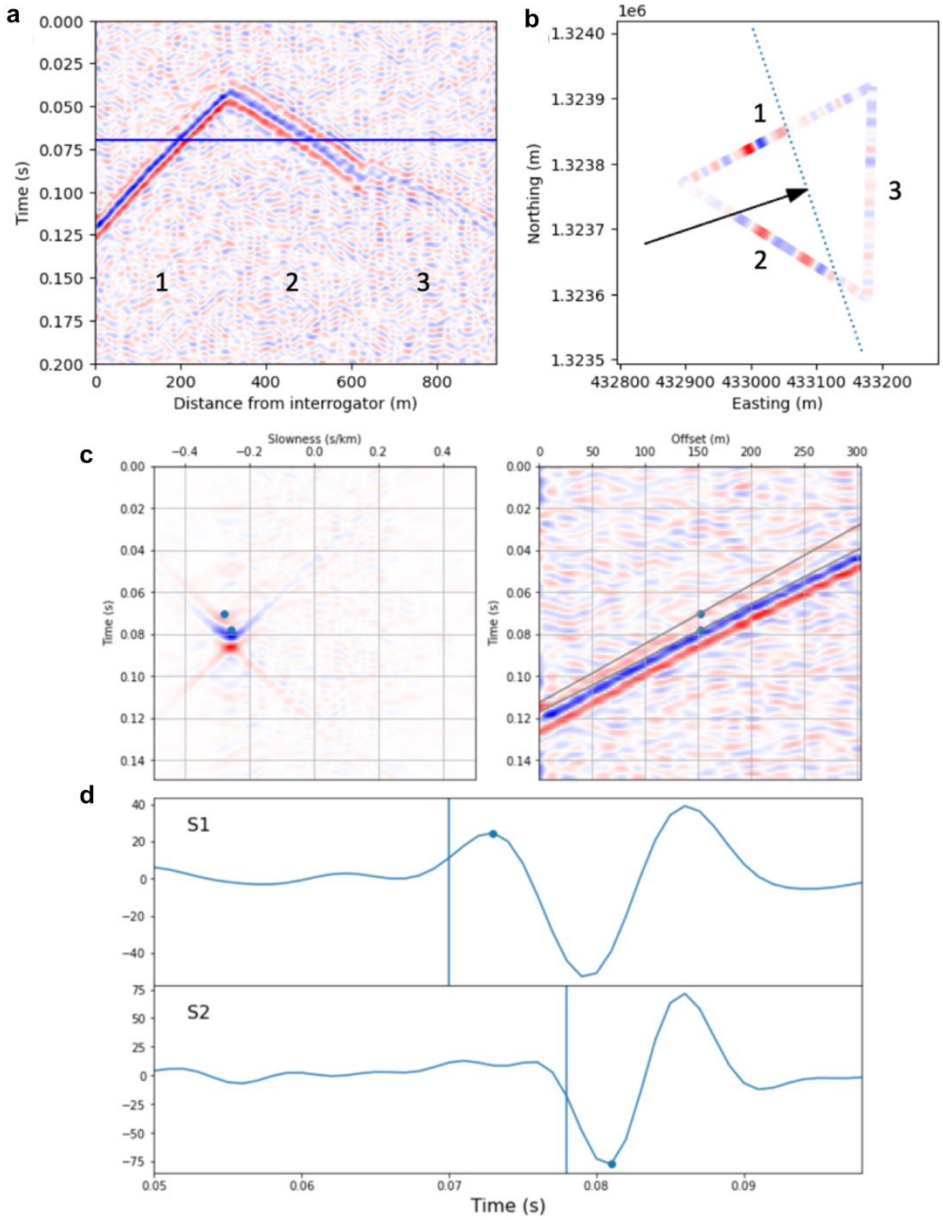

Figure 3. (a) An example recording of an icequake on the triangular DAS array showing the S arrivals. Clear linear moveouts can be observed on the three linear segments of the array. (b) Plot of triangular array geometry with a snapshot of the strain at the time indicated by the blue line in (a). Arrow and dotted line indicates the horizontal projection of the propagation vector and wavefront orientation, respectively, estimated from the slowness analysis. (c)

Slowness analysis of side 1 of the triangular array. Left panel shows a slant stack of the DAS data shown on the right. Two distinct S waves can be observed and picked in the slant stack with travel times corresponding to the midpoint of the linear segment (indicated by blue points). The lines overlaid on the DAS data correspond to the linear moveout indicated by the picked slownesses in the slant stack. (d) Individual traces from the slant stack at the slownesses of the picked arrivals. Vertical lines indicate the travel-time picks from (c), with the blue dots indicating the peak amplitude of the two arrivals which are used in the later polarization analysis.

3 Results

3.1 Detection and location of natural microseismicity using DAS

The first question for the applicability of DAS for studying natural microseismicity is whether one can detect and locate seismicity using DAS alone. To address this question, we compare results of icequakes detected using DAS and geophones separately.

Unlike the three-component geophone records, P-wave arrivals are not visible in our DAS data because only the horizonal component of strain is recorded along the fibre. A near-surface firn layer of substantially lower seismic velocity, refracts P-waves towards vertical incidence. Surface DAS recordings in areas without a firn layer would yield P-wave observations (Walter et al., 2020). However, fast and a slow shear-waves are visible in the DAS data. This is a diagnostic of seismic anisotropy in the ice column, which has been previously documented at Rutford Ice Stream (Harland et al., 2013; Smith et al., 2017) and Korff Ice Rise (Brisbourne et al., 2019). For icequake detection and location, we assume an isotropic fabric, as QuakeMigrate can only pick a single S-wave arrival, typically the fast arrival. This will result in some uncertainty if the slow S-wave arrival is picked instead.

Figure 2 shows the icequake detection results. The line data corresponds to a six-hour period from 0100 to 0700 UTC on 14th January 2020, and the triangle to a six-hour period from 0100 to 0700 UTC on 17th January 2020. Only the hypocentral distance and azimuth are resolved adequately for our DAS geometries. The depths of the DAS-only results are therefore artificially constrained prior to detection and location to between 1700 and 2100 m bsl, based on previous Rutford icequake observations (Hudson et al., 2020; Hudson et al., 2019; Smith et al., 2015). The geophone-only depths are not artificially constrained. The lateral spatial clustering observed in Figure 2 for all network configurations, interpreted to be sticky patches of the bed, is expected from icequake datasets (Hudson et al., 2019; Roeoesli et al., 2016; Smith et al., 2015; Winberry et al., 2009). It shows that both the DAS line and triangle geometries are able to resolve this physical feature in the data, if depths are independently constrained. When DAS and geophone observations are combined, with no artificial depth constraint applied, clustering in depth about the ice bed is also observed (see Figure 2b,c). This demonstrates that surface DAS data can be used in combination with geophones to constrain the hypocentres in three dimensions. Equally, the addition of a vertical section of fibre could also provide depth constraint in the vertical plane, in the same way that the triangle array breaks the symmetry, therefore providing better epicentral constraint in the horizontal plane.

A second observation is that significantly fewer events are detected in data from the DAS-only configuration compared to the geophone-only configuration. Only 499 events are

detected using the DAS triangle, compared to 1321 geophone event detections, and only 139 events are detected using the DAS line, compared to 1270 geophone event detections (see Figure 2d,e,f,g). The line is therefore a less effective configuration than the triangle for event detection, likely due to the two-dimensional nature of the triangle configuration resulting in a higher peak coalescence of energy at a single location, rather than being split by the geometric ambiguity of the line. A spatial detection bias is also apparent in the data, with icequakes from clusters beyond the SW end of the linear DAS configuration detected, but icequakes at closer offsets but perpendicular to the cable not detected. This sensitivity is likely a result of the single component nature of the DAS making it insensitive to certain S phase polarizations.

We also compare the spatial and temporal uncertainty of detected events. Figure 2d and Figure 2f show the epicentral uncertainty of events detected for the line and the triangle, respectively. We compare epicentral uncertainty, rather than hypocentral uncertainty, since the depths of events for the DAS-only detection are artificially constrained. Both the line and the triangle DAS-only epicentral uncertainties are similar to geophone-only detection uncertainties. There are insufficient events detected by the line to quantify whether the triangle or line has better spatial constraint. Figure 2e and Figure 2g show the origin time uncertainty of the events. For both DAS geometries, the geophone-only and DAS-only data suggest similar constraint on the origin time uncertainty.

These results suggest that DAS has limitations for microseismic detection. Firstly, for this experiment arrangement with sources ~2 km below surface, geophones are significantly better than DAS for detecting microseismicity. This is because: (1) the spatial extent of the geophone network is much greater than the DAS (see Figure 2), a limitation specific to our DAS deployment that could be overcome by deploying more fibre; (2) the geophones measure three components of ground motion, and so are sensitive to P-, SV- and SH-phase arrivals; and (3) the geophones have a much lower SNR than single DAS channels. Although the firn velocity structure causes the DAS to be sensitive to only S-phases in this study, horizontally deployed DAS on ice without firn would be sensitive to both P- and S-phases, providing better event depth constraint (Walter et al., 2020). A second limitation is the complexity of combining DAS and geophone data together for detection and location. Theoretically, DAS and geophone data could be combined to reduce spatial and temporal uncertainty. However, there could be a trade-off between the gain of additional observations and detrimental additional noise. Weighting the combined data to mitigate for this is complex, and likely site and network geometry specific. We therefore do not include such an analysis in this study, instead suggesting this as an area for future work. Indeed, the poor performance of our deployment for detection and location is likely due to the spatial extent of the DAS compared to the geophones. We suggest that if the horizontal spatial extent of the DAS is comparable to or greater the spatial extent than the depth of seismicity, then better performance may be achieved, such as in Walter et al. (2020).

Here, we present a migration method that uses input phase picks that are detected on single DAS channels independently from one another. Although this method works, the independent individual channel phase picking method does not fully utilise the high spatial sampling information the DAS offers. Stacking of multiple channels to increase SNR, and/or 2D transform methods might harness the inherently high spatial sampling of DAS to decrease the number of false triggers on individual channels and increase pick accuracy.

3.2 Source and noise spectra

Earthquake spectra can provide insight into both the source physics and ambient noise levels that may hamper the detection of microseismicity. Figure 4a shows the spectra of a 1.5 s event window and two 10 s noise windows for the linear DAS configuration. Figure 4b shows the same time periods, but for a geophone collocated at one end of the DAS fibre.

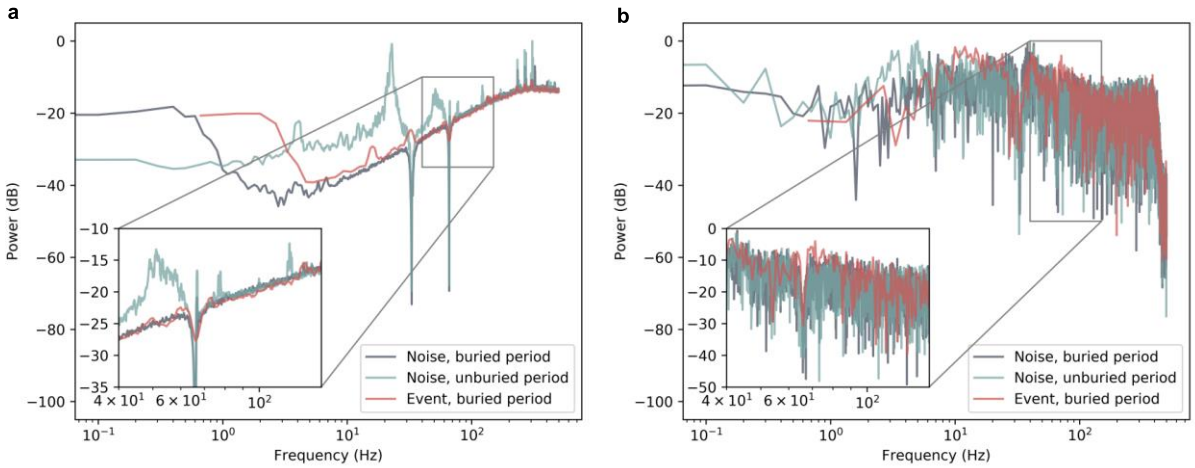

Figure 2. Comparison of event and noise spectra for DAS and geophones. a) Event spectrum and noise spectra while the fibre was unburied and buried for the linear DAS fibre configuration. b) Event spectrum and noise spectra corresponding to the same time periods as in a, but for a geophone collocated at one end of the fibre. Note that the geophone remains buried for the duration of the experiment. Noise windows are of 10 s duration, event windows are of 1.5 s duration.

The two noise periods correspond to times when the fibreoptic cable is unburied and buried a few cm deep, respectively (see Supplementary Figure S1). The DAS spectra above 1 Hz in Figure 4a show that the noise in the unburied DAS data is more than an order of magnitude greater than when it is buried. Geophone data in Figure 4b, confirms that noise conditions are approximately constant over both periods. The increased noise present in the unburied DAS data is interpreted to be due to wind incident on the cable, which is a source of broadband noise and cable resonance with fundamental and higher order modes at 22 Hz and 44 Hz, respectively. During the experiment, the wind speed never exceeded 20 km h^{-1}. This noise is removed by burying the cable.

Paradoxically, the noise for the buried cable is greater below 1 Hz. Burying the cable increases the DAS response over this range by more than 15 dB. This is because the buried cable is coupled to the ice better, and is therefore more sensitive to the primary and secondary microseisms (Cessaro, 1994). Theoretically, the low-frequency DAS instrument response is only limited by the recording duration. For example, Distributed Temperature Sensing (DTS) systems already measure quasi-static strain (Hartog, 2018).

A further feature to note is the pair of minima in the DAS spectra at 33 Hz and 66 Hz. These are a result of 2.5 Hz bandwidth notch filters applied to the data to remove the response of the DAS to surface waves produced by a generator used to power the DAS. This would obviously also affect a geophone collocated next to a generator too, although a generator is not required to power a geophone. Although DAS is sensitive to these

anthropogenic surface waves, mitigating for such signals could be challenging. Indeed, when working in remote areas, a power source for experimental equipment such as the DAS interrogator itself may be required. Whilst surface waves from the generator are detrimental to our study, since they coincide with the S phase arrival of icequakes, these observations positively emphasise the potential of DAS for surface wave studies.

Figure 4 also includes the spectra of an event when the DAS cable is buried. No events are detected when the cable was unburied, and the data in Figure 4a demonstrate why, with the event energy well below the noise threshold of the unburied DAS. The event spectrum observed by the DAS has a higher SNR than the spectrum observed by the geophone. Although a dominant frequency of ~70 Hz is visible in the geophone data, the signal is significantly higher above the noise level in the DAS data, even with a notch filter applied at 66 Hz. This higher spectral SNR is due to the DAS data being stacked over ~1000 channels. It is worth noting that our comparison between DAS and geophones is not strictly fair as stacking hundreds or thousands of geophones over a 1 km length would likely yield a higher SNR spectra than DAS. However, an inherent benefit of DAS is exactly this, in that it allows for thousands of channels to be measured simultaneously and at lower cost. It is also worth noting that the transfer function of the DAS is uncalibrated in this study, and so interpretations of absolute signal amplitudes are therefore limited. However, DAS providers know the transfer function of the interrogator, and if the coupling of fibre to the medium could also be understood, then the fibre-medium coupling transfer function could then be determined.

The resolution, bandwidth and SNR of DAS spectra when buried suggests that DAS is promising for studying the spectra of microseismic sources. The frequency content of a microseismic source allows for limited interpretation of the event source-time function. However, more involved analyses, such as spectral measurement of magnitude (Butcher et al., 2020; Stork et al., 2014), require knowledge of the absolute amplitude of the spectra, in addition to the frequency response of the fibre. This is commonly referred to as the transfer function. Understanding the transfer function of both the interrogator and the fibre-medium coupling should therefore be a priority for studies utilizing DAS, given the potential of DAS for providing higher resolution, bandwidth, and SNR spectra than conventional geophones or broadband seismometers (Lindsey et al., 2020). The advantages of DAS for studying the lower frequency limit of the spectrum also suggest its applicability for ambient noise studies (Ajo-Franklin et al., 2019; Dou et al., 2017; Spica et al., 2020; Zeng et al., 2017). Furthermore, DAS may provide a means of observing other environmental processes with low frequency signals, such as gravity waves in ice shelves (Lipovsky, 2018). The quality of the DAS spectra also prompts the question of whether a spectrum-based earthquake detection method (Hudson et al., 2019) would prove more effective than the QuakeMigrate time-series method. However, this would require averaging the spectrum over many DAS channels, which would reduce the spatial sampling, or increasing the sensitivity of the DAS system to facilitate higher SNR spectra from individual channels.

3.3 Source mechanism inversion

Microseismic source mechanisms are often studied using conventional seismic networks. However, although theory and observations show that DAS has promise for source mechanism analysis (Baird et al., 2020; Karrenbach & Cole, 2020; Vera Rodriguez & Wuestefeld, 2020), a full, quantitative source mechanism inversion has not previously been

attempted for such data. Here, we show an example of a source mechanism inversion using DAS, and compare the result with that of an inversion using conventional seismic instrumentation for the same event. We use the full-waveform method described in Hudson et al. (2020), with further DAS specific considerations described in the Supplementary Information.

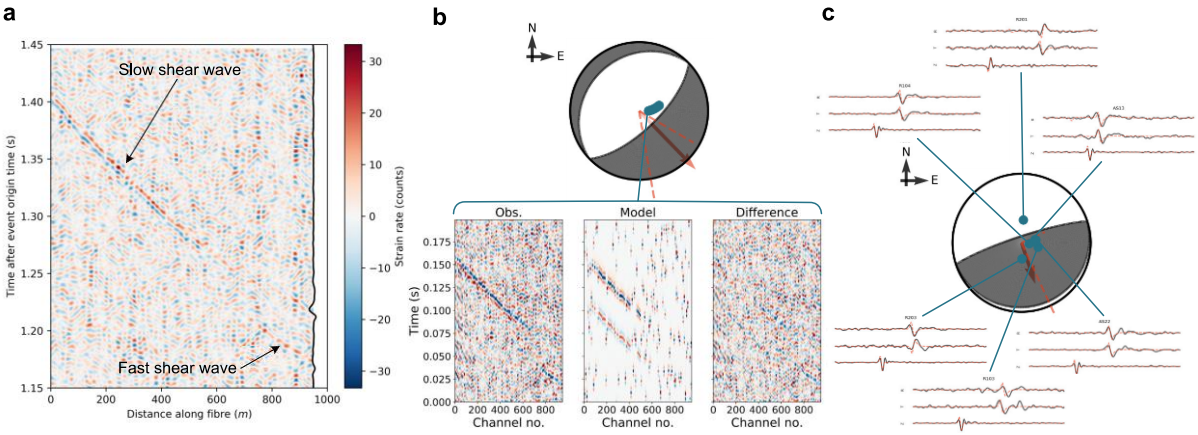

Figure 3. Example of icequake source mechanism inversion results using DAS compared to geophone observations. a) The event S phase arrival at the DAS fibre, colored by strain rate amplitude. The north component of a geophone collocated at one end of the fibre is shown by the black line at ~950 m. Key features of the event arrival are labelled. b) Double-Couple (DC) constrained full-waveform source mechanism inversion result using the DAS fibre observations, showing the observed waveforms used in the inversion, the modelled result, and the difference, colored by normalized strain rate. The blue scatter points on the focal mechanism plot indicate the fibre and the red solid arrow and dashed lines indicate the slip vector and its associated uncertainty, respectively. c) DC constrained full-waveform source mechanism inversion result using geophone observations. The Z components include the P phase arrival only, and the R and T components include the S phase arrival only. Note that the Z and RT components are not temporally aligned with one another. Both focal mechanism radiation patterns are for an upper hemisphere projection for P-wave radiation, for consistency with other similar studies. Both inversions used 10^6 samples of the model space.

The source mechanism inversion results for the icequake highlighted by the yellow star in Figure 2 are shown in Figure 5. This icequake occurs when the DAS is configured in a linear arrangement. Source mechanism results for additional icequakes are provided in the Supplementary Information. Figure 5a shows the event arrival at every channel along the DAS cable. The fast shear wave is dominant at smaller epicentral distances, with the slow shear wave prevalent at greater distances. The north component of a collocated geophone at the SW end of the linear cable is shown in black, at its approximate location. Figure 5b shows the DAS source mechanism inversion result. The double-couple (DC) upper hemisphere focal mechanism is as one might expect (Hudson et al., 2020; Smith et al., 2015), suggesting horizontal slip with the slip vector aligned approximately with the ice flow direction (see Figure 2). Uncertainty in the slip vector, shown by the red dashed lines, is of the order of $\pm 20°$. It should be noted that a P-wave radiation pattern is plotted for consistency with other studies, although the fibre, and hence the inversion, is actually only sensitive to S-wave arrivals. Due to the 45° rotation of the S-wave radiation pattern relative to the P radiation pattern, the DAS cable lies near an S-wave radiation pattern maximum. The fit between the

model and the observations is quantified by a variance reduction value of 0.65. The 2D observation, model, and difference fields show that the model provides a good fit, with negligible discernible coherent energy shown in the difference field. The scatter in the best fitting model result is due to the automatic alignment algorithm not correctly aligning every individual channel to the data. However, the general trend and the small proportion of scatter relative to fitted signal provides us with confidence that the inversion is successful. To our knowledge this is the first microseismic source mechanism inversion performed using DAS observations.

For comparison, we also show DC-constrained moment tensor source inversion results using geophones instead of DAS. All P-phase polarities are correctly fitted by the geophones, as are the majority of S-phase polarities, although there is more uncertainty for the S-wave matches due to some of the shear wave splitting not being entirely compensated for. Unfortunately, geophone coverage of the focal sphere for the network configuration is not as well configured for source mechanism analysis as previous studies (Hudson et al., 2020; Kufner et al., n.d.; Smith et al., 2015), leaving the most likely DC source poorly constrained compared to previous observations. While the slip vector is approximately the direction of ice flow, and therefore in agreement with the DAS source inversion, the uncertainty, denoted by the dashed lines, indicates $\sim 270°$ azimuthal uncertainty. This is significantly greater than the $\sim 45°$ azimuthal uncertainty for the DAS source inversion. These results show that DAS provides better constraint of the source mechanism than the geophone network configuration, at least for this icequake.

Although the DAS source mechanism inversion outperforms the geophone inversion here, there are a number of challenges and limitations of the inversion. The first limitation is that due to the low velocity firn layer, body wave phases arrive approximately vertically. This means that DAS is not sensitive to P-wave arrivals that have particle motions perpendicular to the fibre, unlike studies with no firn layer (Walter et al., 2020), and so the source mechanism can only be constrained using S-waves. Comparing DAS strain-rate observations to model outputs can also be challenging. While some models output strain-rate, the results from the wave propagation code used here, fk (Zhu & Rivera, 2002), have to be converted from velocities. Even if the model used did output strain-rate directly, one still needs to simulate gauge-length effects. Another challenge is accounting for any anisotropy at the study site. Our results suggest that we have adequately accounted for anisotropy, but our method only holds for anisotropy path effects that can be approximated as homogenous on the spatial scale of the cable. If anisotropy were present at the source, or varied and was unknown across the length of the cable, then our method would be invalid. However, one could instead view the clear anisotropy observations in Figure 5a as an advantage of DAS, as an inversion for ice fabric anisotropy is theoretically possible.

Here, we have treated the DAS and geophone data separately for the source mechanism inversions to provide a clear comparison between DAS and geophones. However, it is theoretically possible to combine DAS and geophone observations in a joint inversion. While this would not provide substantial gains for the event discussed here due to little increase in spatial constraint over the focal sphere, it might in other situations. One could imagine constraining the inversion better by deploying DAS within the centre of a network and geophones located more sparsely and at greater distances, for example. Performing such a joint inversion would provide its own challenges, such as how to weight DAS and geophone observations, since SNR and the single-component vs. three-components may introduce bias into the solution.

3.4 Seismic shear-wave splitting inversion

Here we show how the triangular DAS array can be used as a multi-component sensor to measure shear-wave splitting due to anisotropy in the ice column. This example event is found to have a shear-wave splitting delay time of 0.0093 s, based on averaging all three vertices of the triangular array to estimate the splitting at the centre of the array (see Figure 3d). We find a best fitting propagation azimuth of 72˚, as indicated by the arrow in Figure 3b, with horizontal slownesses of 0.28 s/km and 0.26 s/km for the fast and slow waves, respectively. Furthermore, we estimate an a ray emergence inclination of ~22–25˚ based on an estimate of a mean firn layer S velocity of 1456 m s^{-1} (Smith et al., 2015). However, we expect that the true inclination may be steeper than this, due to a non-linear gradient in the firn layer velocity structure. This is evidenced by the lack of P wave sensitivity. We find that reducing the inclination modulates the magnitude of the strain recorded but has only a minor effect on the relative strain sensitivity patterns observed, so we do not believe that uncertainty in emergence angle will be a significant source of error.

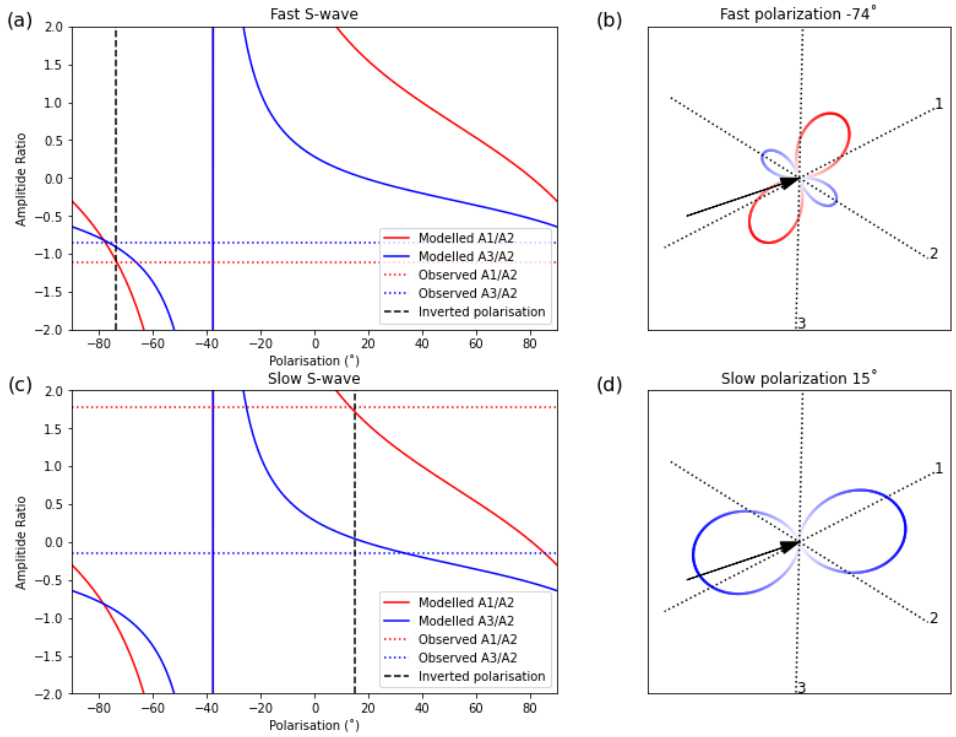

Figure 4. a) Results of the polarization inversion of the fast S-wave. Solid lines indicate modelled amplitude ratios as a function of polarization angle, dotted horizontal lines indicated the measured amplitude ratios and vertical dashed black line indicates the inverted polarization (-74˚). (b) Predicted strain sensitivity pattern for the inverted fast S arrival with polarization of 74˚. Dotted lines indicate the orientation of the three sides of the array, and black arrow indicates the horizontal projection of the propagation direction. (c) and (d) same as (a) and (b) but for the slow S-wave with inverted polarization of 15˚.

The S-wave polarisation inversion results for the fast and slow S-wave for this example icequake are shown in Figure 6, along with the modelled strain sensitivity pattern of the best fitting inversion results. The best fit solution for the fast S-wave polarisation, ϕ_f,

is -74˚, where ϕ_f is defined in the ray frame according to the convention of Wuestefeld et al. (2010) (i.e. ϕ_f is 0˚ for SV and ±90˚ for SH, clockwise along the ray towards the source). The best fit solution for the slow S-wave polarization is 15˚. The observation that the fast and slow S-wave polarisations, ϕ_f, are approximately perpendicular gives us confidence that this method is correctly measuring shear wave splitting.

We compare this splitting measurement with that of a previous study at Rutford (Smith et al., 2017) by converting our splitting fast-slow delay time into a S-wave velocity difference, dv_s. From the estimated source location for the event and assuming a straight-line path between source and receiver, we estimate a dv_s of 0.78% with an average inclination of 29˚. Although Smith et al. (2017) found some splitting as high as 4-5%, they also found that dv_S and ϕ_f varied substantially for different azimuths and inclinations, due to the orthorhombic symmetry of the anisotropy. If we restrict comparison of our results to only splitting parameters from Smith et al. (2017) with ray paths within azimuthal and inclination ranges of ±13˚ of our measurement, they have a mean dv_S and ϕ_f of 0.84% and -73˚, respectively. These are remarkably similar to our result.

The consistency between our result and previously published results gives us confidence in our approach, suggesting that smaller 2D DAS arrays can be effectively used as multicomponent sensors to detect and quantify shear wave splitting. Practically, however, this is unlikely to become the preferred method of characterising shear wave splitting. Deploying a DAS system in a small azimuthally varying 2D array removes one of the major benefits of DAS systems: their large aperture, instead effectively reducing the array to a point sensor. In our case the source-receiver geometry is such that the ray path sampled a relatively weak splitting axis, producing a splitting measurement not very representative of the broader anisotropic fabric. In contrast, a less dense but broader aperture geophone array could record multiple splitting measurements from a single event, covering a wide range of azimuths and inclinations, which would provide a more comprehensive picture of the anisotropy. Nevertheless, we suggest there could be benefits of including small azimuthally varying 2D segments of DAS arrays as part of a larger aperture deployment to introduce some multi-component sensitivity.

4 Considerations for future DAS deployments

One advantage of DAS is the high-density spatial sampling of the microseismic wavefield, which can provide much higher resolution spectral data and higher resolution sampling of the radiation pattern of an earthquake, compared to conventional networks. Limitations of DAS include practical limitations on the spatial extent of cables, the single component nature of the strain measurement, and the limited amplitude sensitivity leading to low SNR on individual channels. With this and evidence from this study in mind, we suggest the following considerations for future surface DAS experiments. (1) Consider hybrid geophone and DAS networks for microseismic detection. (2) Use cable lengths comparable to or greater than the source depths to be studied. This might be logistically challenging for remote sites. (3) Orient the cable in multiple directions, or use multiple cables with time-synchronised interrogators. Breaking the symmetry of a DAS system can improve detection at different azimuths. (4) Isolate the cable from wind-shear and other surface noise. Cables could be buried or placed in conduits. (5) Consider the wavelength of sources being studied, ensuring that the gauge-length is less than half the wavelength, for adequate Nyquist sampling. In our study, basal icequake S waves typically have wavelengths of ~25 m, which

is greater than twice the gauge-length. (6) Deployment in a borehole. Advantages of this would include being sensitive to P waves and increased SNR. However, deployment in a single, vertical borehole would result in complete azimuthal ambiguity in source location. Ideally, one would deploy DAS horizontally and vertically for increased sensitivity and hypocentral constraint.

As well as the aforementioned considerations for utilising current DAS technology, there are also technological developments that would improve DAS for natural microseismic study applications. Firstly, the gauge-length imposes a limit on the ability to observe high frequency, near source observations. The ability to vary gauge-length during an experiment, or use of a chirp-style signal to instantaneously measure multiple gauge-lengths may prove useful for certain investigations. Secondly, greater amplitude resolution would have been beneficial in our study, where we typically have signals no greater than ± 40 counts. This is already technologically possible, with engineered fibre DAS systems, such as Silixa's Carina system, now providing several orders of magnitude improvements in sensitivity compared to the system used in this study. A more significant improvement might be the development of readily available helically wound fibre to measure strain in three dimensions (Baird, 2020; Lim Chen Ning & Sava, 2018). This may allow for greater sensitivity of P-wave observations for various cable orientations or shallow velocity structures. However, helically wound fibre would conversely affect the sensitivity to S-waves, possibly negating any advantages of enhanced P-wave sensitivity. Practically, DAS interrogators currently consume considerable power and the interrogator is expensive compared to geophones or standard seismometers. Reducing power consumption and unit cost would allow DAS to be deployed in more remote locations and for longer periods of time than in this study. However, even without such improvements to DAS interrogators, the fibre itself is relatively inexpensive, allowing for intermittent long-term monitoring of a site.

5 Conclusions

DAS provides dense spatial sampling of seismic wavefields and therefore has significant potential for studying natural microseismicity. We investigate the potential of DAS deployed on the Earth's surface. We show that DAS alone is relatively poor at detecting and locating seismicity compared to geophone observations, when deployed with an aperture less than the depth of the earthquake hypocentres being studied. However, DAS can outperform geophones in other analysis of natural microseismic sources. The SNR and bandwidth of the spectrum measured by stacking a number of DAS channels is significantly improved over a single geophone, and likely seismometers, especially for low, near quasi-static frequencies. Obtaining the DAS transfer function would allow the use of spectral observations to constrain moment magnitude of microseismicity. We also demonstrate that the dense spatial sampling that DAS provides can constrain source mechanism inversions better than conventional geophone networks, at least for our specific source-receiver geometry. Finally, we show that for a 2D fibre geometry, it is possible to quantify the shear-wave-splitting exhibited due to anisotropy in the ice column. In summary, whilst DAS has significant potential for natural microseismicity studies, it also has limitations. Any future study should consider utilizing the strengths of DAS to address the underlying science question, but also include conventional seismometers to compensate for the limitations of DAS, in a complementary, hybrid deployment.

Acknowledgements

We thank NERC British Antarctic Survey for logistics and field support. This work was funded by a NERC Collaborative Antarctic Science Scheme grant (grant number CASS-166). Geophones were deployed as part of the BEAMISH project, and were borrowed from the UK Geophysical Equipment Facility (GEF loan number 1111). We thank Silixa for the loan of an iDAS interrogator. The seismic data will be made available through IRIS and the UK Polar Data Centre. The microseismic detection software used is QuakeMigrate, which is open source software that is detailed in Hudson et al. (2019) and Smith et al. (2020). The moment tensor source inversion python software used is SeisSrcInv, which is deposited on Zenodo (Hudson, 2020a). The moment magnitude calculation python code used in this study, SeisSrcMoment, is also deposited on Zenodo (Hudson, 2020b). GMT was used in the production of the map figure (Wessel et al., 2019).

References:

Ajo-Franklin, J. B., Dou, S., Lindsey, N. J., Monga, I., Tracy, C., Robertson, M., et al. (2019). Distributed Acoustic Sensing Using Dark Fiber for Near-Surface Characterization and Broadband Seismic Event Detection. *Scientific Reports*, *9*(1), 1–14. https://doi.org/10.1038/s41598-018-36675-8

Allen, R. V. (1978). Automatic earthquake recognition and timing from single traces. *Bulletin of the Seismological Society of America*, *68*(5), 1521–1532.

Baird, A. F., Stork, A. L., Horne, S. A., Naldrett, G., Kendall, J.-M., Wookey, J., et al. (2020). Characteristics of microseismic data recorded by distributed acoustic sensing systems in anisotropic media. *GEOPHYSICS*, *85*(4), KS139–KS147. https://doi.org/10.1190/geo2019-0776.1

Baird, Alan F. (2020). Modelling the Response of Helically Wound DAS Cables to Microseismic Arrivals. In *First EAGE Workshop on Fibre Optic Sensing* (pp. 1–5). European Association of Geoscientists & Engineers. https://doi.org/10.3997/2214-4609.202030019

Benioff, H. (1935). A linear strain seismograph. *Bulletin of the Seismological Society of America*, *25*(4), 288–288.

Booth, A. D., Christoffersen, P., Schoonman, C., Clarke, A., Hubbard, B., Law, R., et al. (2020). Distributed Acoustic Sensing (DAS) of Seismic Properties in a Borehole drilled on a Fast-Flowing Greenlandic Outlet Glacier. *Geophysical Research Letters*, 0–3. https://doi.org/10.1029/2020gl088148

Brisbourne, A. M., Martín, C., Smith, A. M., Baird, A. F., Kendall, J. M., & Kingslake, J. (2019). Constraining Recent Ice Flow History at Korff Ice Rise, West Antarctica, Using Radar and Seismic Measurements of Ice Fabric. *Journal of Geophysical Research: Earth Surface*, *124*(1), 175–194. https://doi.org/10.1029/2018JF004776

Butcher, A., Luckett, R., Kendall, J.-M., & Baptie, B. (2020). Seismic magnitudes, corner frequencies and microseismicity: Using ambient noise to correct for high-frequency attenuation.

Capon, J. (1969). High-resolution frequency-wavenumber spectrum analysis. *Proceedings of the IEEE*, *57*(8), 1408–1418.

Cessaro, R. K. (1994). Sources of primary and secondary microseisms. *Bulletin - Seismological Society of America*, *84*(1), 142–148.

Daley, T. M., Miller, D. E., Dodds, K., Cook, P., & Freifeld, B. M. (2016). Field testing of modular borehole monitoring with simultaneous distributed acoustic sensing and geophone vertical seismic profiles at Citronelle, Alabama. *Geophysical Prospecting*,

64(5), 1318–1334. https://doi.org/10.1111/1365-2478.12324

Daley, Thomas M., Freifeld, B. M., Ajo-Franklin, J., Dou, S., Pevzner, R., Shulakova, V., et al. (2013). Field testing of fiber-optic distributed acoustic sensing (DAS) for subsurface seismic monitoring. *Leading Edge*, *32*(6), 699–706. https://doi.org/10.1190/tle32060699.1

Dean, T., Cuny, T., & Hartog, A. H. (2017). The effect of gauge length on axially incident P-waves measured using fibre optic distributed vibration sensing. *Geophysical Prospecting*, *65*(1), 184–193. https://doi.org/10.1111/1365-2478.12419

Dou, S., Lindsey, N., Wagner, A. M., Daley, T. M., Freifeld, B., Robertson, M., et al. (2017). Distributed Acoustic Sensing for Seismic Monitoring of the Near Surface: A Traffic-Noise Interferometry Case Study. *Scientific Reports*, *7*(1), 1–12. https://doi.org/10.1038/s41598-017-11986-4

Geiger, L. (1912). Probability method for the determination of earthquake epicenters from the arrival time only. *Bull. St. Louis Univ*, *8*(1), 56–71.

Harland, S. R., Kendall, J.-M., Stuart, G. W., Lloyd, G. E., Baird, A. F., Smith, A. M., et al. (2013). Deformation in Rutford Ice Stream, West Antarctica: measuring shear-wave anisotropy from icequakes. *Annals of Glaciology*, *54*(64), 105–114. https://doi.org/10.3189/2013AoG64A033

Hartog, A. H. (2018). *An Introduction to Distributed Optical Fibre Sensors*. Taylor & Francis Group. Retrieved from https://books.google.co.uk/books?id=aVmWnQAACAAJ

Hudson, T. (2020). TomSHudson/SeisSrcInv: Initial release for publication. Zenodo. https://doi.org/10.5281/zenodo.3726697

Hudson, T.S. (2020a). TomSHudson/SeisSrcInv: Initial release for publication (Version v1.0.0-beta). *Zenodo*. https://doi.org/http://doi.org/10.5281/zenodo.3726697

Hudson, T.S. (2020b). TomSHudson/SeisSrcMoment: First formal release (Version 1.0.0). *Zenodo*. https://doi.org/http://doi.org/10.5281/zenodo.4010325

Hudson, T S, Brisbourne, A. M., Walter, F., Gräff, D., White, R. S., & Smith, A. M. (2020). Icequake Source Mechanisms for Studying Glacial Sliding. *Journal of Geophysical Research: Earth Surface*, *125*(11). https://doi.org/10.1029/2020JF005627

Hudson, Thomas S, Smith, J., Brisbourne, A., & White, R. (2019). Automated detection of basal icequakes and discrimination from surface crevassing. *Annals of Glaciology*, *60*(79), 1–11.

Innanen, K. A., Lawton, D., Hall, K., Bertram, K. L., Bertram, M. B., & Bland, H. C. (2019). Design and deployment of a prototype multicomponent distributed acoustic sensing loop array. In *SEG Technical Program Expanded Abstracts 2019* (pp. 953–957). https://doi.org/10.1190/segam2019-3216304.1

Jousset, P., Reinsch, T., Ryberg, T., Blanck, H., Clarke, A., Aghayev, R., et al. (2018). Dynamic strain determination using fibre-optic cables allows imaging of seismological and structural features. *Nature Communications*, *9*(1), 2509. https://doi.org/10.1038/s41467-018-04860-y

Karrenbach, M., & Cole, S. (2020). DAS microseismic source mechanism estimation by forward-modeling. *SEG International Exposition and Annual Meeting 2019*, 1004–1008. https://doi.org/10.1190/segam2019-3216570.1

Karrenbach, M., Cole, S., Ridge, A., Boone, K., Kahn, D., Rich, J., et al. (2019). Fiber-optic distributed acoustic sensing of microseismicity, strain and temperature during hydraulic fracturing. *GEOPHYSICS*, *84*(1), D11–D23. https://doi.org/10.1190/geo2017-0396.1

Kufner, S.-K., Brisbourne, A. M., Smith, A. M., Hudson, T. S., Murray, T., Schlegel, R., et al. (n.d.). Not all icequakes are created equal: Diverse bed deformation mechanisms at Rutford Ice Stream, West Antarctica, inferred from basal seismicity. *Journal of Geophysical Research: Earth Surface Earth Surface*.

https://doi.org/10.1002/essoar.10504915.1
Li, Z., & Zhan, Z. (2018). Pushing the limit of earthquake detection with distributed acoustic sensing and template matching: A case study at the Brady geothermal field. *Geophysical Journal International*, *215*(3), 1583–1593. https://doi.org/10.1093/gji/ggy359
Lim Chen Ning, I., & Sava, P. (2018). High-resolution multi-component distributed acoustic sensing. *Geophysical Prospecting*, *66*(6), 1111–1122. https://doi.org/10.1111/1365-2478.12634
Lindsey, N. J., Craig Dawe, T., & Ajo-Franklin, J. B. (2019). Illuminating seafloor faults and ocean dynamics with dark fiber distributed acoustic sensing. *Science*, *366*(6469), 1103–1107. https://doi.org/10.1126/science.aay5881
Lindsey, N. J., Rademacher, H., & Ajo-Franklin, J. B. (2020). On the Broadband Instrument Response of Fiber-Optic DAS Arrays. *Journal of Geophysical Research: Solid Earth*, *125*(2), 1–16. https://doi.org/10.1029/2019JB018145
Lipovsky, B. P. (2018). Ice Shelf Rift Propagation and the Mechanics of Wave-Induced Fracture. *Journal of Geophysical Research: Oceans*, *123*(6), 4014–4033. https://doi.org/10.1029/2017JC013664
Lomax, A., & Virieux, J. (2000). Probabilistic earthquake location in 3D and layered models. *Advances in Seismic Event Location, Volume 18 of the Series Modern Approaches in Geophysics*, 101–134.
Marra, G., Clivati, C., Luckett, R., Tampellini, A., Kronjäger, J., Wright, L., et al. (2018). Ultrastable laser interferometry for earthquake detection with terrestrial and submarine cables. *Science*, *361*(6401), 486–490. https://doi.org/10.1126/science.aat4458
Martin, E. R., Huot, F., Ma, Y., Cieplicki, R., Cole, S., Karrenbach, M., & Biondi, B. L. (2018). A Seismic Shift in Scalable Acquisition Demands New Processing: Fiber-Optic Seismic Signal Retrieval in Urban Areas with Unsupervised Learning for Coherent Noise Removal. *IEEE Signal Processing Magazine*, *35*(2), 31–40. https://doi.org/10.1109/MSP.2017.2783381
Masoudi, A., & Newson, T. P. (2016). Contributed Review: Distributed optical fibre dynamic strain sensing. *Review of Scientific Instruments*, *87*(1). https://doi.org/10.1063/1.4939482
Mateeva, A., Lopez, J., Potters, H., Mestayer, J., Cox, B., Kiyashchenko, D., et al. (2014). Distributed acoustic sensing for reservoir monitoring with vertical seismic profiling. *Geophysical Prospecting*, *62*(4), 679–692. https://doi.org/10.1111/1365-2478.12116
Parker, T., Shatalin, S., & Farhadiroushan, M. (2014). Distributed Acoustic Sensing – a new tool for seismic applications. *First Break*, *32*(2010), 61–69. https://doi.org/10.3997/1365-2397.2013034
Rignot, E., Mouginot, J., & Scheuchl, B. (2011). Ice Flow of the Antarctic Ice Sheet. *Science*, *333*(6048), 1427–1430. https://doi.org/10.1126/science.1208336
Roeoesli, C., Helmstetter, A., Walter, F., & Kissling, E. (2016). Meltwater influences on deep stick-slip icequakes near the base of the Greenland Ice Sheet. *Journal of Geophysical Research: Earth Surface*, 1–18. https://doi.org/10.1002/2015JF003601
Sladen, A., Rivet, D., Ampuero, J. P., De Barros, L., Hello, Y., Calbris, G., & Lamare, P. (2019). Distributed sensing of earthquakes and ocean-solid Earth interactions on seafloor telecom cables. *Nature Communications*, *10*(1), 1–8. https://doi.org/10.1038/s41467-019-13793-z
Smith, A. M. (2006). Microearthquakes and subglacial conditions. *Geophysical Research Letters*, *33*(24), 1–5. https://doi.org/10.1029/2006GL028207
Smith, E.C., Smith, A. M., White, R. S., Brisbourne, A. M., & Pritchard, H. D. (2015). Mapping the ice-bed interface characteristics of Rutford Ice Stream, West Antarctica, using microseismicity. *Journal of Geophysical Research: Earth Surface*, *120*(9), 1881–

1894. https://doi.org/10.1002/2015JF003587
Smith, Emma C., Baird, A. F., Kendall, J. M., Martin, C., White, R. S., Brisbourne, A. M., & Smith, A. M. (2017). Ice fabric in an Antarctic ice stream interpreted from seismic anisotropy. *Geophysical Research Letters*, *44*(8), 3710–3718. https://doi.org/10.1002/2016GL072093
Smith, J. D., White, R. S., Avouac, J.-P., & Bourne, S. (2020). Probabilistic earthquake locations of induced seismicity in the Groningen region, the Netherlands. *Geophysical Journal International*, *222*(1), 507–516. https://doi.org/10.1093/gji/ggaa179
Spica, Z. J., Perton, M., Martin, E. R., Beroza, G. C., & Biondi, B. (2020). Urban Seismic Site Characterization by Fiber-Optic Seismology. *Journal of Geophysical Research: Solid Earth*, *125*(3), 1–14. https://doi.org/10.1029/2019JB018656
Stork, A. L., Verdon, J. P., & Kendall, J. M. (2014). The robustness of seismic moment and magnitudes estimated using spectral analysis. *Geophysical Prospecting*, *62*(4), 862–878. https://doi.org/10.1111/1365-2478.12134
Stork, Anna L., Baird, A. F., Horne, S. A., Naldrett, G., Lapins, S., Kendall, J.-M., et al. (2020). Application of Machine Learning To Microseismic Event Detection in Distributed Acoustic Sensing (Das) Data. *Geophysics*, 1–53. https://doi.org/10.1190/geo2019-0774.1
Vera Rodriguez, I., & Wuestefeld, A. (2020). Strain microseismics: Radiation patterns, synthetics, and moment tensor resolvability with distributed acoustic sensing in isotropic media. *Geophysics*, *85*(3), KS101–KS114. https://doi.org/10.1190/geo2019-0373.1
Verdon, J. P., Horne, S. A., Clarke, A., Stork, A. L., Baird, A. F., & Kendall, J.-M. (2020). Microseismic monitoring using a fibre-optic Distributed Acoustic Sensor (DAS) array. *Geophysics*, *85*(3), 1–48. https://doi.org/10.1190/geo2019-0752.1
Walter, F., Gräff, D., Lindner, F., Paitz, P., Köpfli, M., Chmiel, M., & Fichtner, A. (2020). Distributed Acoustic Sensing of Microseismic Sources and Wave Propagation in Glaciated Terrain. *Nature Communications*, *53*(9), 1689–1699. https://doi.org/10.1017/CBO9781107415324.004
Wang, H. F., Zeng, X., Miller, D. E., Fratta, D., Feigl, K. L., Thurber, C. H., & Mellors, R. J. (2018). Ground motion response to an ML 4.3 earthquake using co-located distributed acoustic sensing and seismometer arrays. *Geophysical Journal International*, *213*(3), 2020–2036. https://doi.org/10.1093/GJI/GGY102
Wessel, P., Luis, J. F., Uieda, L., Scharroo, R., Wobbe, F., Smith, W. H. F., & Tian, D. (2019). The Generic Mapping Tools Version 6. *Geochemistry, Geophysics, Geosystems*, *20*(11), 5556–5564. https://doi.org/10.1029/2019GC008515
Winberry, J. P., Anandakrishnan, S., Alley, R. B., Bindschadler, R. A., & King, M. A. (2009). Basal mechanics of ice streams: Insights from the stick-slip motion of Whillans Ice Stream, West Antarctica. *Journal of Geophysical Research*, *114*, 1–11. https://doi.org/10.1029/2008JF001035
Withers, M., Aster, R., Young, C., Beiriger, J., Harris, M., Moore, S., & Trujillo, J. (1998). A comparison of select trigger algorithms for automated global seismic phase and event detection. *Bulletin of the Seismological Society of America*, *88*(1), 95–106.
Wuestefeld, A., Al-Harrasi, O., Verdon, J. P., Wookey, J., & Kendall, J. M. (2010). A strategy for automated analysis of passive microseismic data to image seismic anisotropy and fracture characteristics. *Geophysical Prospecting*, *58*(5), 755–773. https://doi.org/10.1111/j.1365-2478.2010.00891.x
Zeng, X., Lancelle, C., Thurber, C., Fratta, D., Wang, H., Lord, N., et al. (2017). Properties of noise cross-correlation functions obtained from a distributed acoustic sensing array at Garner Valley, California. *Bulletin of the Seismological Society of America*, *107*(2), 603–610. https://doi.org/10.1785/0120160168

Zhan, Z. (2019). Distributed acoustic sensing turns fiber-optic cables into sensitive seismic antennas. *Seismological Research Letters*, *91*(1), 1–15. https://doi.org/10.1785/0220190112

Zhu, L., & Rivera, L. A. (2002). Computation of dynamic and static displacement from a point source in multi-layered media. *Geophysical Journal International*, *148*, 619–627.